Impact of a Lisbon-type tsunami on the U.K. coastline and the implications for tsunami propagation over broad continental shelves

K. J. Horsburgh,[1] C. Wilson,[1] B. J. Baptie,[2] A. Cooper,[3] D. Cresswell,[3] R. M. W. Musson,[2] L. Ottemöller,[2] S. Richardson,[3] and S. L. Sargeant[2]

[1]   We investigate the propagation of tsunamis toward the European shelf break, using six different initial conditions (based on the 1755 Lisbon earthquake), in order to assess the hazard to this region. Only one of our source models, an assumed earthquake magnitude of 8.7 Mw with a zonal fault orientation, resulted in significant wave heights at the U.K. coastline. Because of wave spreading, only a fraction of the tsunami energy from such an event reaches the northwest European shelf, which itself provides a further buffer through reflection and frictional dissipation. However, we found significant local reamplification due to wave interactions and resonance on the continental shelf. The maximum elevations obtained were comparable to severe winter storm conditions, but with extreme local variability in the tsunami amplitude. Our results suggest that the impact of any repeat of this event would be very sensitive to the precise location and orientation of the source deformation, as well as by complex topographic interactions on the shelf. The uncertainties arising from the combination of source orientation and bathymetric interaction suggest that any assessment of risk, for places where tsunamis are likely, should consider a large ensemble of initial conditions.

1.   Introduction

[2]   The 26 December 2004 Sumatra-Andaman earthquake (9.0–9.3 Mw) and the resultant tsunami was one of the worst modern, natural disasters. It prompted governments and international agencies to reevaluate the likelihood, and consequences, of similar events occurring elsewhere [*Kanamori*, 2006]. The risk to the United Kingdom (and more generally to coasts surrounding the northwest European seaboard) was assessed in a study [*Kerridge et al.*, 2005] that concluded the probability of any such event is very low. However, there is historical and geological evidence of tsunamis reaching northern European shores [e.g., *Smith et al.*, 2004; *Dawson et al.*, 2000] so the possibility of future events affecting low-lying populations in this region cannot be dismissed. This paper investigates the hazard to the United Kingdom associated with a tsunami similar to that generated by the Lisbon 1755 earthquake. We consider the effects of topographic steering for this scenario, the regions of energy dissipation, and the implications for tsunamis on broad shelves elsewhere.

[3]   We select the Azores-Gibraltar fault zone (AGFZ) as the source region, since this was the source of the tsunami in 1755 which (along with the earthquake) destroyed the city of Lisbon [see, e.g., *Baptista et al.*, 1998a]. It was also the source of the well-documented 1969 (7.9 Mw) earthquake [*Fukao*, 1973]; small-amplitude (0.2 m) waves with tsunami periodicities were recorded at Newlyn, United Kingdom, following that event [*Dawson et al.*, 2000]. Similar waves were recorded at Newlyn after earthquakes west of Portugal in 1941 (8.2 Ms), and 1975 (7.9 Ms). *Kerridge et al.* [2005] concluded that this region is the most probable source for a major North Atlantic tsunami. There is, of course, geological evidence of a major tsunami impacting the northern coastline of the United Kingdom following the Storrega submarine landslide approximately 8000 years ago [e.g., *Bondevik et al.*, 1997; *Smith et al.*, 2004], but it is widely thought that the marine deposition required for any repeat occurrence could only accrue during a glacial period [*Rise et al.*, 2005].

[4]   Following the Lisbon earthquake of 1 November 1755 there were reports of tsunami waves as high as 10 m along the coasts of Portugal, Spain, and Morocco [*Baptista et al.*, 1998a] and there is one account of 3 m waves reaching Cornwall in the United Kingdom [*Borlase*, 1755]. Although the historical data is summarized by *Baptista et al.* [1998a], locating the epicenter of the 1755 earthquake is difficult. Conflicting information regarding the distribution of intensities, origin time, and tsunami arrivals [*Johnston*, 1996; *Mendes et al.*, 1999], and the diffuse distribution of earthquakes along this part of the AGFZ [*Zitellini et al.*, 2001], lead to large uncertainties, and

---

[1]Proudman Oceanographic Laboratory, Liverpool, UK.
[2]British Geological Survey, Edinburgh, UK.
[3]HR Wallingford, Wallingford, UK.

the range of possible epicenters spans around 500 km (see Figure 1b). Modeling of both the tsunami [*Baptista et al.*, 1998b] and earthquake intensity [*Johnston*, 1996] has been used to estimate the location and the size of the source. Detailed geophysical surveying in the eastern section of the AGFZ has taken place [*Zitellini et al.*, 1999, 2001], but no single location has been implicated. This is not surprising since even for the better observed 28 February 1969 tsunami, neither direct numerical simulation [*Gjevik et al.*, 1997] or adjoint methods using observations [*Pires and Miranda*, 2001] were able to determine unique source parameters.

[5] Since the exact source of the 1755 earthquake remains unknown we consider three possible fault orientations and locations, which we discuss in section 2. Source dimensions and average slip are derived from realistic assumptions of the earthquake magnitude and empirical relationships for the source scaling of intraplate earthquakes. We do not consider the subduction model of *Gutscher* [2004] since there is significant evidence against subduction [e.g., *Stich et al.*, 2005]. Composite source models [e.g., *Vilanova et al.*, 2003] are also excluded. It is not the intention of this paper to explore the relative merits of the various postulated sources for the 1755 tsunami; rather, we use the historical information as a first-order check on model performance in order to explore the hazards and oceanographic implications associated with this scenario.

2. Source Strength and Location

[6] Estimates of the magnitude of the 1755 earthquake generally vary between 8.5 and 9.0 Mw. *Johnston* [1996] used isoseismals to determine the moment magnitude, finding a best fit of 8.7 ± 0.39 Mw. In this study we select lower and upper estimates as 8.3 and 8.7 Mw, respectively, on the basis of *Abe* [1979]. We assume that the 1755 earthquake ruptured the entire seismogenic zone (between 60 km depth and the surface). With a fault dip of about 50° [*Fukao*, 1973] this means that a realistic fault width is 60 km/(sin 50°), or about 75 km. We assume an intraplate tectonic setting [*Johnston*, 1996] and propose three plausible models for fault orientations and locations. Scaling relationships for intraplate earthquakes imply larger slip compared to interplate earthquakes of the same dimensions [*Scholz et al.*, 1986; *Scholz*, 2002]. The models are described below and their physical source dimensions are given in Table 1. The various locations can be found in Figure 1a.

[7] Model A has the same epicenter as the 1969 earthquake in the Horseshoe Abyssal Plain, to the southeast of the Gorringe Bank [*Fukao*, 1973]. The origin of this earthquake is reasonably well understood. It has a thrust mechanism on a fault plane that dips to the north and is related to the tectonic uplift of the Gorringe Bank. The fault orientation is favorable to compression in northwest-southeast direction. The model provides a good fit for the macroseismic data; the Horseshoe Fault is an active tectonic feature; and there is significant seismic activity in this area. However, *Baptista et al.* [1998b] suggest that sources analogous to the 1969 earthquake do not reproduce the observed distribution of wave heights and traveltimes along the Iberian coast for the 1755 event.

[8] Model B is an earthquake north of the Gorringe Bank as suggested by *Johnston* [1996], occurring on a thrust fault that dips to the south and is related to the tectonic uplift of the bank. This is similar to the top hat model of *Gjevik et al.* [1997], which assumes uplift of the Gorringe Bank ridge as a source although there is evidence (N. Zitellini, unpublished data, 2005) to suggest that it is inactive. As a fault plane solution we used the south dipping auxiliary plane of the *Fukao* [1973] model for the 1969 event. Model C is equivalent to the N160 model of *Baptista et al.* [1998b]. The source location is closer to the Iberian shore than either of the other models, between the Gorringe Bank and the edge of the continental shelf west of Cape San Vicente. The earthquake occurs on a thrust fault dipping to the northeast. *Baptista et al.* [1998b] found that this model produced tsunami arrival times that better matched the historical reports. However, the underlying tectonics of such a model are less well defined. The inclusion of this model allowed us to examine the effect of source orientation on tsunami waves reaching the coastlines of the United Kingdom, Ireland, and northwest Europe.

[9] In each case, the sea bed displacement due to an inclined, rectangular fault was calculated using the well-known analytical expressions of *Okada* [1985]. These formulae assume the Earth to be a homogeneous elastic half-space and require the source parameters given in Table 1. We have assumed the worst case of complete crustal rupture: solutions with a specified focal depth would give smaller displacements. The sea floor deformations obtained were mapped directly onto the sea surface as shown in Figure 2. There are deficiencies in this assumption, as pointed out by *Gjevik et al.* [1997] who employed a nonhydrostatic model and showed that in certain circumstances the maximum surface elevation can be 30% less than the displacement at the sea bed. Neither can the surface deformation contain the discontinuity that is present at the precise line of a fault. Our modeling scheme introduced the deformation as a sea surface elevation and, in practice, the discontinuity was slightly smoothed because of regridding.

3. Numerical Modeling

[10] The models described in this section are nonlinear, shallow water (NLSW) models which are a routine and

Figure 1. (a) Bathymetry (m) used in numerical model simulations. Key locations are annotated as follows: GS (Goban Spur), GR (Galician Rise), F (Figuera), SV (San Vincente), GB (Gorringe Bank), C (Cadiz), HAP (Horseshoe Abyssal Plain), and M (Madeira). Also shown is the region covered by the Telemac model (dashed), the region of the seafloor perturbations described later in the text (solid, red), and two regions used for energy diagnostics (solid, blue and green). (b) Map of the Azores-Gibraltar Fault Zone, east of the Madeira Tore rise, with annotated faults. Red circles denote earthquake epicenters, including various epicenters proposed for the 1755 earthquake: Ma: *Machado* [1966]; Mi: *Milne* [cited by *Johnston*, 1996]; Mo: *Moreira* [1989]; Re: *Reid* [1914]; Zi: *Zitellini et al.* [1999]. Earthquake epicenters from the BGS World Seismicity Database [*Henni et al.*, 1998] are also plotted.
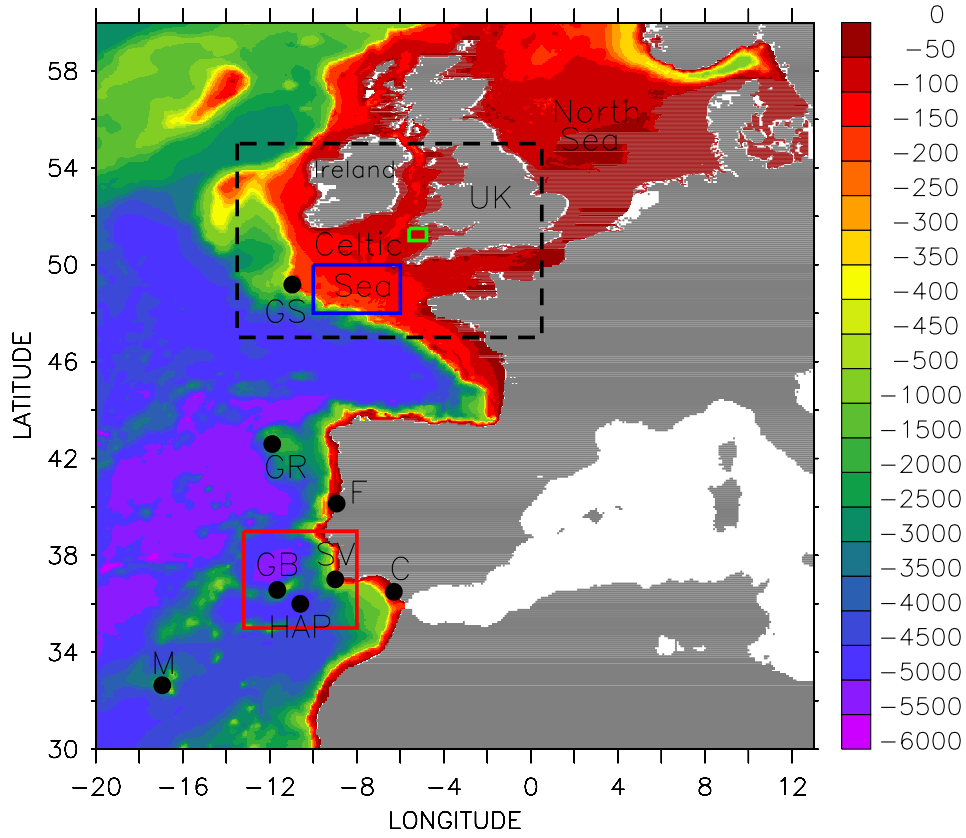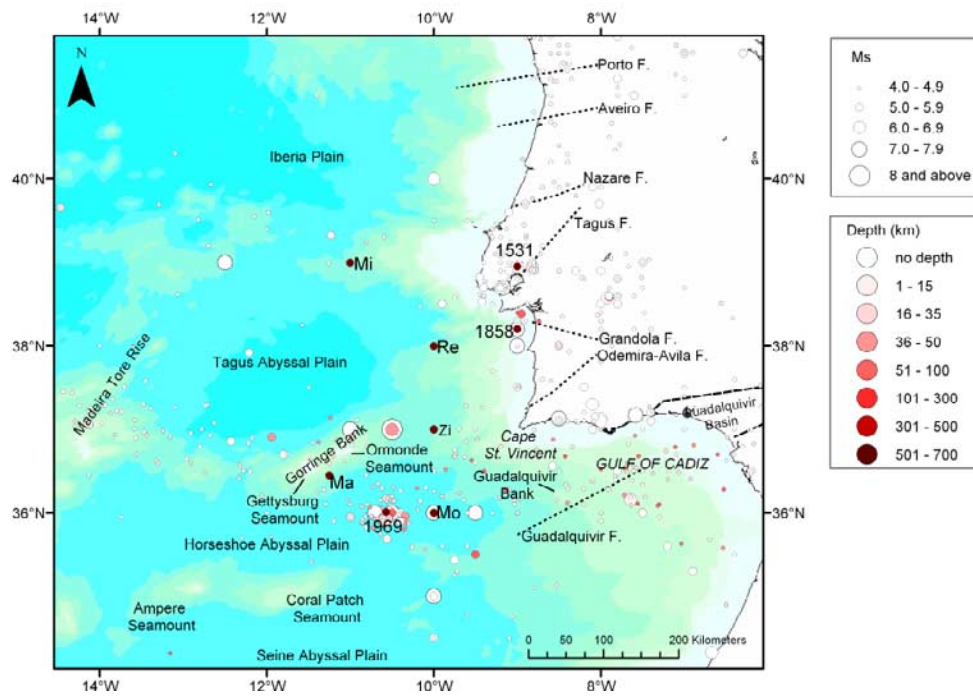
Figure 1

Table 1. Models of Fault Location and Orientation and Physical Source Dimensions[a]

	Model A		Model B		Model C	
Fault plane Strike/dip/rake	235/52/73		81/41/110		340/45/90	
Fault center	36.01°N, 10.57°W		37.00°N, 11.50°W		37.00°N, 9.75°W	
	Southeast of Gorringe Bank		North of Gorringe Bank		Southwest of Lisbon	
Source model	A1	A2	B1	B2	C1	C2
Magnitude	8.3 Mw	8.7 Mw	8.3 Mw	8.7 Mw	8.3 Mw	8.7 Mw
Length (km)	105	210	105	210	105	210
Width (km)	75	75	75	75	75	75
Mean slip (m)	6.8	13.6	6.8	13.6	6.8	13.6
Seismic moment, M_0 (Nm)	3.5×10^{21}	1.4×10^{22}	3.5×10^{21}	1.4×10^{22}	3.5×10^{21}	1.4×10^{22}

[a]Calculations assume the shear modulus, $\mu = 6.5 \times 10^{11}$ dyn cm^{-2} [*Johnston*, 1996], and the scaling factor for intraplate earthquakes, $\alpha = 6.5 \times 10^{-5}$ [*Scholz*, 2002].
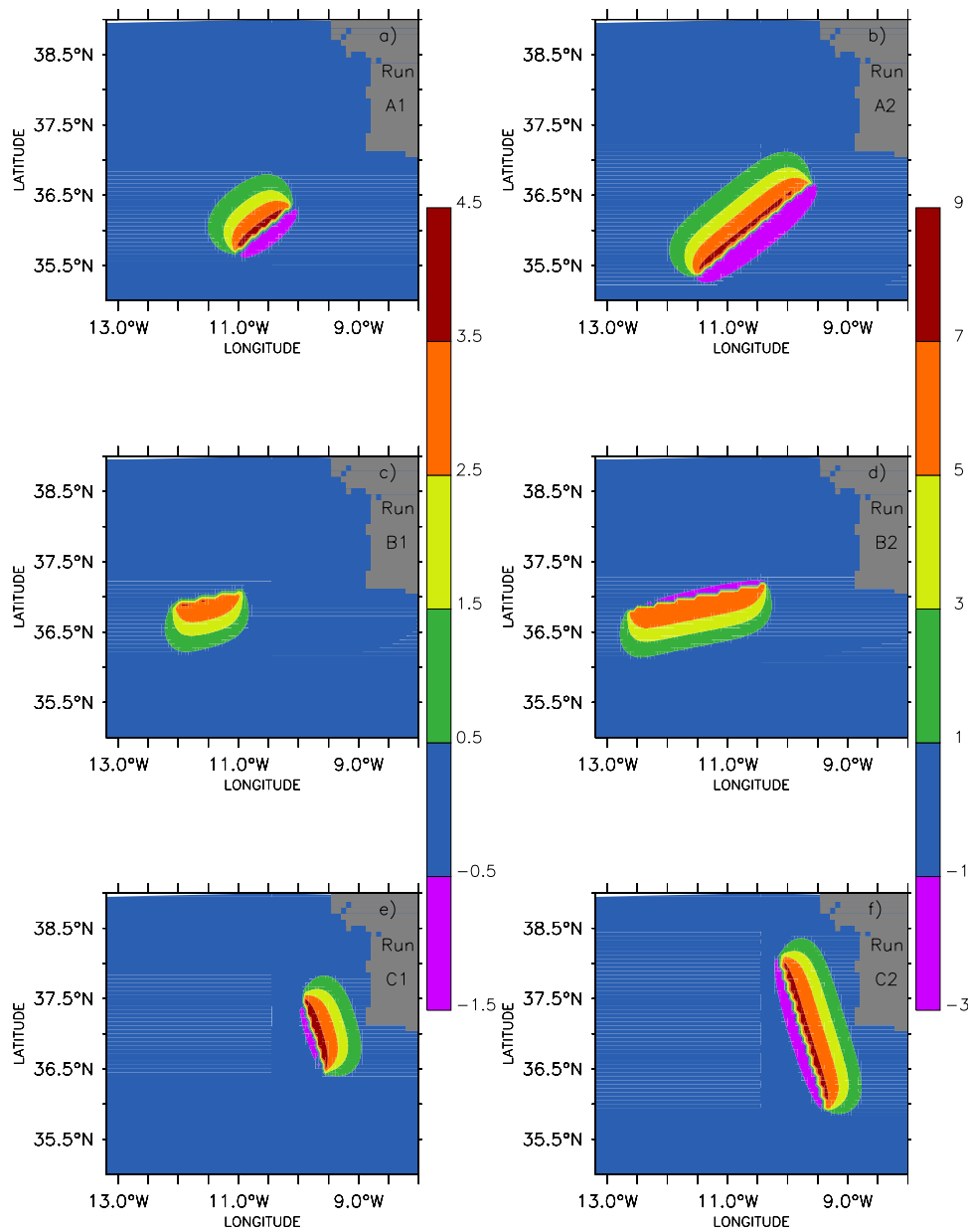
Figure 2. Tsunamigenic seafloor movement scenarios (m), used to perturb the sea surface of the model simulations. Scenarios A, B, and C explore different epicenter locations and fault orientations in the *Okada* [1985] model. Group 1 (left) corresponds to a magnitude of 8.3 Mw, and group 2 (right) corresponds to 8.7 Mw.

appropriate choice for tsunami propagation modeling away from the immediate source, so long as the wavelength is properly discretized [*Shuto*, 1991]. The widely used MOST model [*Titov and Gonzalez*, 1997] is of this type. Recent comparisons of model predictions with reliable coastal observations in the Sea of Japan [*Choi et al.*, 2003] also show that nested, finite difference, NLSW models produced accurate simulations of coastal inundation and runup. For optimum discretization, in this study we nested an unstructured finite element model within a wide domain finite difference model.

3.1. Finite Difference Modeling

[11] In order to best represent the tsunamis at their origin, as well as their subsequent evolution across the European Shelf, we extended the U.K. operational storm surge model [*Flather*, 2000] to cover the region 20°W to 13°E, 30°N to 60°N. The model solves the two-dimensional shallow water equations in finite difference form in spherical coordinates, with a quadratic formulation for stress at the sea bed and radiation conditions at the open lateral boundaries. The resolution used here was 1/30° latitude by 1/20° longitude, resulting in an approximately 3.5 km horizontal grid that provides effective discretization and avoids numerical dispersion [*Shuto*, 1991; *Kowalik*, 2001]. The model integrations ran at a time step of 10 s for 12 h, by which time the wave train had passed the United Kingdom. Elevations and velocity fields were archived every minute for subsequent diagnostics. As well as examining maximum elevations and tsunami arrival times we studied wave energetics, making the connection between the genesis region and the subsequent modification of the wave as it propagates.

3.2. Energetics

[12] We derive an energy equation from the shallow water governing equations in spherical coordinates. The continuity and momentum equations used in the model can be found in the work of *Flather* [1976] and are written concisely below. For completeness we retained the Coriolis and advective terms possessed by the model, although it is well known that these terms are negligible for tsunamis. Similarly, the tan φ term arises from the transformation to spherical coordinates; it is numerically insignificant and is included only for mathematical exactness.

$$\frac{\partial \eta}{\partial t} + \nabla_S \cdot (H\mathbf{u}) = 0 \qquad (1)$$

$$\frac{\partial \mathbf{u}}{\partial t} + \mathbf{u} \cdot \nabla_S \mathbf{u} + \left(f + \frac{u}{R}\tan\phi\right)\mathbf{k} \times \mathbf{u} = -g\nabla_S\eta + \frac{\gamma}{H}\mathbf{u}|\mathbf{u}| + A\nabla_S^2\mathbf{u} \qquad (2)$$

where η is the elevation of sea surface; $\nabla_S \cdot \mathbf{V} = \frac{1}{R\cos\varphi}\left(\frac{\partial V_\chi}{\partial\chi} + \frac{\partial}{\partial\varphi}(V_\varphi \cos\varphi)\right)$ defines the horizontal divergence operator in spherical coordinates for a vector, $\mathbf{V}$; $H = h + \eta$ is the total depth of water; $\mathbf{u}$ is the horizontal velocity field; R is the radius of the Earth; f is the Coriolis parameter; $\nabla_S C = \left(\frac{1}{R\cos\varphi}\frac{\partial C}{\partial\chi}, \frac{1}{R}\frac{\partial C}{\partial\varphi}\right)$ defines the gradient operator for a scalar, C; χ is eastward longitude, φ is northward latitude; $\mathbf{k}$ is the unit radial vector; g is the acceleration due to gravity; γ is a

coefficient of bottom friction, with a value of 0.0025; and $A(H)$ is a depth-dependent horizontal eddy viscosity. In this study, where unresolved eddy motions are not relevant, the role of the final term in equation (2) is simply to suppress numerical noise at smaller scales.

[13] The energy equation is found by taking the scalar product of (2) with $\mathbf{u}$. After some manipulation, this gives the flux form of the energy equation:

$$\frac{\partial E}{\partial t} + \nabla_S \cdot \mathbf{F_E} = \rho\gamma|\mathbf{u}|^3 + \rho(\mathbf{u}H)\cdot A\nabla_S^2\mathbf{u} \qquad (3)$$

where ρ is density, $E = \rho(HK + \frac{1}{2}g\eta^2)$ is the total energy per unit horizontal area; $K = \frac{1}{2}|\mathbf{u}|^2$ is the kinetic energy density; and $\mathbf{F_E} = \rho\mathbf{u}H(K + g\eta)$ is the total energy flux per unit length normal to the flux. Although we have derived the expression from the governing equations, the energy flux term, $\mathbf{F_E}$, is identical to the time-mean form arising from linear theory that has been widely used in the study of tidal energy fluxes [e.g., *Davies and Kwong*, 2000]. We find that time integrals of $\mathbf{F_E}$ have only a very small contribution from the kinetic energy component, of the order 1% (in agreement with shallow water theory). The first term on the right-hand side of equation (3) represents dissipation from bottom friction, which we show is small but not insignificant in shallow water. The viscosity term (which arises from the parameterization of Reynolds stresses in the equations) was 5 orders of magnitude smaller than the main terms and is not considered further.

[14] Equation (3) states that the rate of change of total energy per unit horizontal area depends on the divergence of the energy flux as well as dissipation from frictional processes. The energy flux itself would reveal the transfer of energy from one place to another, but not necessarily whether the energy changes locally. It is only when this flux diverges, for instance, when the flow interacts with topography, that the total energy changes locally. It is possible to show that the energy flux divergence can be split into one term containing the divergence of advected energy and another containing the local gradient in bathymetry.

[15] We inserted the six different source models shown in Figure 2 into the finite difference model and denoted these Runs A1–C2. Each of these is a gridded version of the analytical solution [*Okada*, 1985] of the seafloor disturbance, and they explore the variation of epicenter, fault orientation, and earthquake magnitude. The simulations included tides inherently, but tidal signals were removed from the following results. We found the dynamical interaction between tides and tsunamis to be insignificant. The state of the tide is obviously crucial when determining the total water level at coastal locations but, for the purposes of risk assessment, tide and tsunami can be superimposed. Each scenario was also simulated with the finite element model, but only Run B2 is shown.

3.3. Finite Element Modeling

[16] To simulate the tsunami propagation to the shoreline it was necessary to develop a finer grid model of the United Kingdom and Irish coasts. The waves simulated here had typical periods of approximately 20 min, and it was beneficial to use a variable grid model, allowing the number of cells per wavelength to remain approximately constant. This
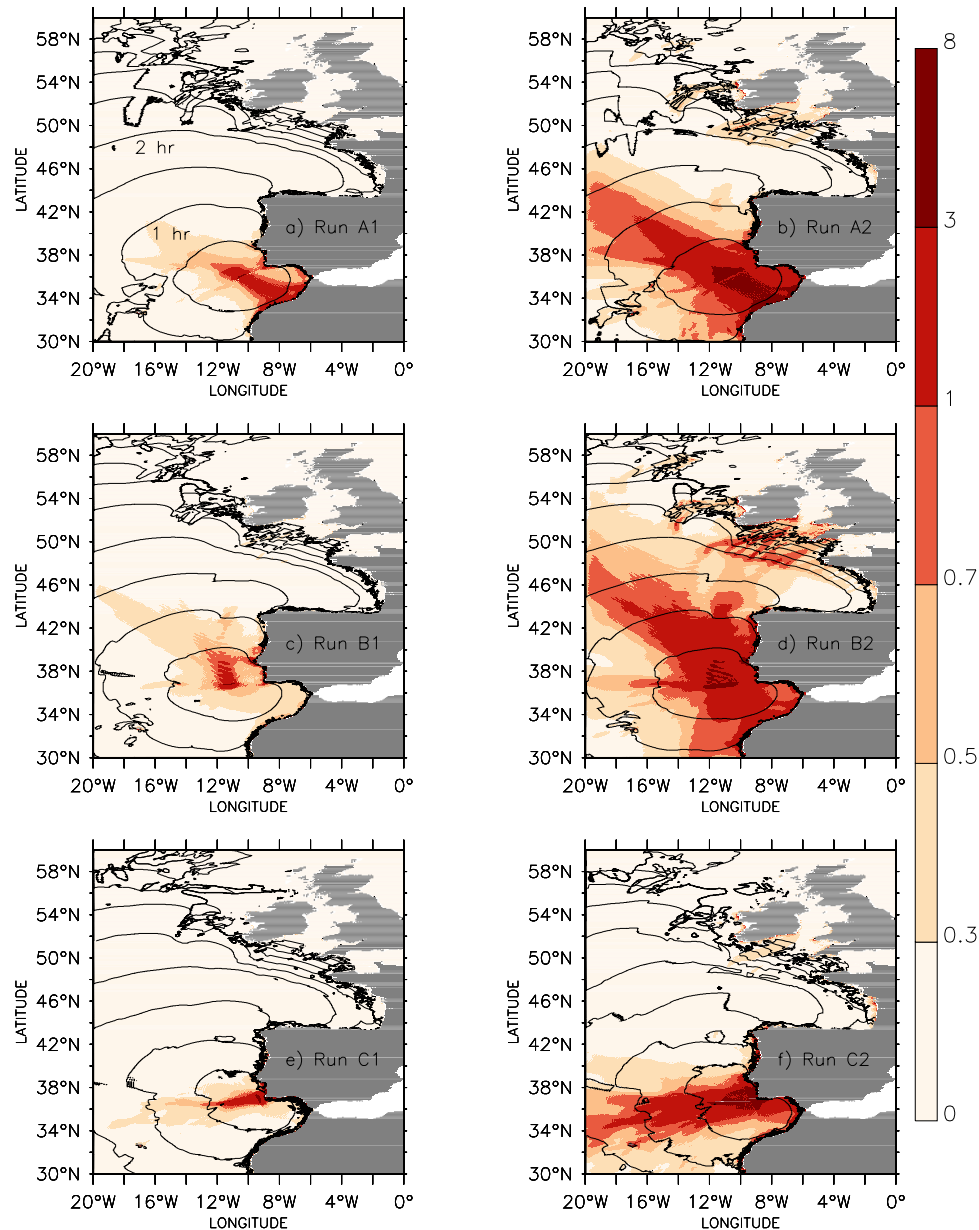
Figure 3. Maximum sea surface elevation during the first 12 h (shaded, m) and arrival time of maximum for the first 6 h (contours, 0.5 h contour interval) corresponding to the seafloor perturbations A1–C2.

variable mesh was generated using the TELEMAC-2D hydrodynamic model [*Galland et al.*, 1991; *Hervouet*, 2000a]. This model has been extensively validated for tides [*Malcherek*, 2000; *Sauvaget et al.*, 2000; *Jones and Davies*, 2005] and wind-induced response [*Jones and Davies*, 2006] in shallow shelf seas. Its capacity to simulate runup well is aided by a wetting-drying scheme that performs well at the finest resolution [*Jones and Davies*, 2006]. In dam break tests the inundating flood wave celerity is accurate to 3% [*Hervouet*, 2000b], and numerical dispersion is minimal, even for highly distorted tidal estuaries [*Malcherek*, 2000].

[17] The model mesh was set up using the spherical coordinates option and, for consistency, the TELEMAC-2D runs used the same bathymetric data as the wide domain model. The inner domain was nested in the region indicated by the dashed line in Figure 1 and contained 46,000 nodes and 88,000 elements whose mesh size varied from 10 km at the outer boundary to less than 1 km near to the United Kingdom and Irish coasts. Radiation boundary conditions were imposed on all open boundaries (to allow any outwardly directed energy to leave the domain); the incident tsunami was imposed as a time series of elevations and depth-averaged currents from the outer model at the southern and western boundaries. The simulation ran for 12 h after the initial disturbance, and bed friction was represented as a Nikuradse roughness length [e.g., *Soulsby*, 1998] of 0.01 m.

4. Results

[18] The contours of arrival time and maximum elevation obtained at each cell are shown in Figure 3 for the six runs,

Table 2. Comparison of Simulated Arrival Times With the Observational Reports

Location	Latitude (°N)	Longitude (°W)	Observed Arrival Time (min)[a]	Arrival Time (min)[b] for Modeled Scenario					
				A1	A2	B1	B2	C1	C2
Figuera	40.14	8.88	45 ± 10	72	67	67	65	69	59
S. Vincente	37.01	8.99	16 ± 7	15	12	19	14	2	2
Cadiz	36.50	6.30	78 ± 15	70	69	77	72	63	56
Madeira	32.63	16.88	90 ± 15	61	54	61	55	76	74

[a]*Baptista et al.* [1998a].
[b]The time the model elevation first exceeds 0.2 m, rounded to the nearest minute.

A1–C2. The patterns of maximum elevation are different for each variant of orientation/location (A, B, and C), although the times of arrival are broadly similar. It is evident that the precise nature of the seafloor perturbation is the largest uncertainty in the effects of the tsunami. For example, Run A2 (Figure 3b) has maximum elevation along a line normal to its fault line, northwestward into the North Atlantic and southeastward toward Africa, with little effect on the shallow shelf seas to the north. Run B2 (Figure 3d) also has maximum elevation along a line normal to the source model fault line, which is now rotated slightly clockwise; this run has maximum elevations of up to 1 m focused in beams in the Celtic Sea. In contrast, Run C2 (Figure 3f), whose fault line is oriented almost normal to that of Run B2, has maximum elevation along a line between Iberia and the mid-Atlantic. The lower-magnitude, 8.3 Mw, scenarios (Figure 3, left) have a similar pattern to the higher-magnitude, 8.7 Mw, scenarios (Figure 3, right), but are typically 1–3 m near their source, compared to 3–8 m for the latter. Kinks in the arrival time contours result from modification to the wave speed as it propagates over topographic features.

[19] Table 2 compares the arrival time of the modeled waves with the best interpretation [*Baptista et al.*, 1998a] of literature describing the 1755 Lisbon tsunami. There are differences between each of the six scenarios, and these differences vary by location. For example, the "observed" arrival time of 16 ± 7 min at S. Vincente is well-matched by the A and B runs, but not by the C runs, whose arrival time is much shorter. Our modeled arrival times agreed with those of *Baptista et al.* [1998b], where the seismic assumptions were similar, but like them we found that no single model run could reconcile apparently contradictory observations. Our model is in broad agreement with the historical information (particularly along the Iberian coastline where reports were more likely to be accurate) and with previous attempts to numerically model the event. The sensitivity of arrival time to the initial conditions is demonstrated with these six runs. We make no further attempt to qualify the various sources but now concentrate on run B2 which develops the largest elevation amplitudes at the U.K. continental shelf break, and has the most significant implications for hazard.

[20] The evolution of the tsunami in Run B2 is shown in Figure 4 as a sequence of sea surface elevations. After 10 min (Figure 4a) the wave amplitude is typically greater than 0.25 m and is still several meters in places. Our results are similar to those of *Gjevik et al.* [1997] who obtained a large primary crest, followed by a weaker trough, in their simulations of the 1969 event. The complex shape of the evolving waves comes from the (primarily) gravitational adjustment of the initial condition. After 30 min (Figure 4b), the first tsunami wave has reached the Iberian peninsula and wave crest refraction is evident. To the west, the wave crest has become discontinuous; to the north, wave amplitude remains locally greater than 1.25 m. After 60 min (Figure 4c), the first positive tsunami wave has hit North Africa and the Strait of Gibraltar. The northernmost part of the wave crest is significantly refracted as it encounters the Galician Rise (see Figure 1a for location).

[21] The leading wave reaches the U.K. shelf edge after 120 min (Figure 4d), and it also refracts into the Bay of Biscay. Upon encountering the shallow shelf, the wavelength reduces and the amplitude increases as the wave shoals. Local amplitudes are in the range 0.25 m to 1.25 m. Comparison of the leading wave height at two points along 8° W (one in 4000 m depth, the other 200 m) showed approximately a two-fold amplification. This agrees well with a simple calculation of wave energy flux per unit wave crest (Green's Law), which predicts amplification of $(4000/200)^{0.25}$, a factor of 2.1. As the tsunami propagates further across the U.K. shelf into the Irish Sea, by 180 min (Figure 4e) an obvious cusp forms in the wave crest near the Goban Spur. By 240 min (Figure 4f) the small-scale features on the U.K. shelf have interacted with the wave to give a diffraction-like pattern, which is consistent with the elevation maxima described previously (Figure 3d).

[22] The finite element model run confirmed that scenario B2 had the most significant impact on the U.K. and Irish coasts. Figure 5 shows the free surface elevation at 5 and then 8 h after the initial disturbance. The finite element model produced the same beams of maximum elevation, confirming the results of the finite difference model and giving confidence in the physical nature of the phenomenon. Wave amplitudes of 0.5–1.0 m were observed in the finite element model once the tsunami passed onto the continental shelf, but before it encountered very shallow water. The traveltime of the primary wave to the southwest tip of the United Kingdom was 264 min, similar to the 268 min of *Baptista et al.* [1998b]. The wave period at this point was found to be approximately 20 min which is consistent with the anecdotal reports of *Borlase* [1755]. Figure 5b shows that after 8 h there is still much energy in the system, and a confused sea surface has resulted from complex reflections and interactions in shallow water. This regional ringing and slow decay of energy was also observed by *Fine et al.* [2005] during their simulations of a tsunami entering Canada's Burin inlet. The near-coast maximum elevations are shown in Figure 6a. The effects of the tsunami locally are due to focusing mechanisms and local reamplification, determined by the resonances of different bays and inlets. The majority of the south coast of Ireland, and a large part the Cornish coast in the southwest of the United Kingdom, recorded elevations in excess of 1 m at some time during the model run, and several locations had maxima exceeding 3.5 m. To show the very local nature of these effects, wave maxima were extracted along a coastal perimeter segment and are shown in Figure 6b.
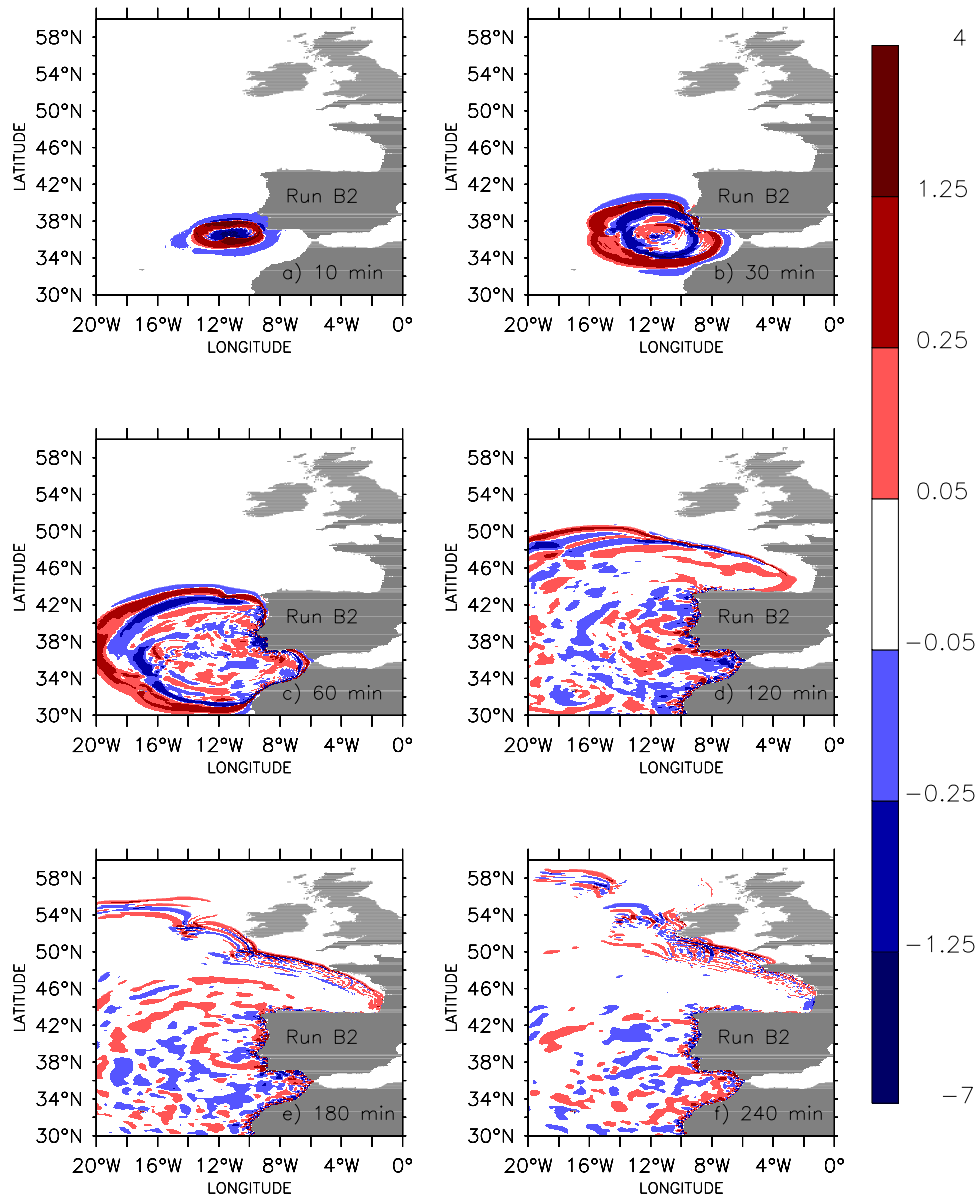
Figure 4. Sequence of snapshots of sea surface elevation (m) for Run B2: (a) 10 min; (b) 30 min; (c) 60 min; (d) 120 min; (e) 180 min; (f) 240 min.

[23] To examine the degree to which the shelf break features were responsible for the beams of maximum elevation, the shelf edge bathymetry was smoothed in the along-slope direction, while maintaining its across-slope profile to avoid changing any shoaling effects (Figure 7a). As can be seen in Figure 4c, the tsunami also interacts with the larger-scale (order 200 km) bathymetric feature of the Galician Rise, therefore we also synthesized a bathymetry with the Galician Rise removed for depths less than 4200 m (Figure 7b). These two sensitivity experiments complement each other in that different length scales were considered, and the bathymetric adjustments were applied in regions of contrasting depth. The run with smoothed shelf edge bathymetry no longer has beams of high maximum elevation (Figure 8a), but instead the maximum elevation decreases uniformly as the wave passes over the continental shelf, until reamplification occurs in the very nearshore.

Also note the uniformity of the arrival time contours on the shelf, because the tsunami now approaches as a plane wave. There is a separate beam of maximum elevation originating from the Goban Spur, where constructive interference between the two wavefronts still occurs. Figure 8b shows the maximum elevations from the computation with the Galician Rise removed. There is now a region of substantially increased maximum elevation, typically 0.7 m to 1 m, compared to the results in Figure 3d. This increased wave height eventually impacts on the U.K. shelf, amplifying the pattern of beams seen in the original run.

[24] The maximum elevation is a useful diagnostic for studying the potential impacts of the tsunami, but does not contain detailed information about the path or transformation of the wave. The time-mean energy flux, however, shows how the energy spreads from the tsunamigenic region and is guided through the system. For periodic processes it
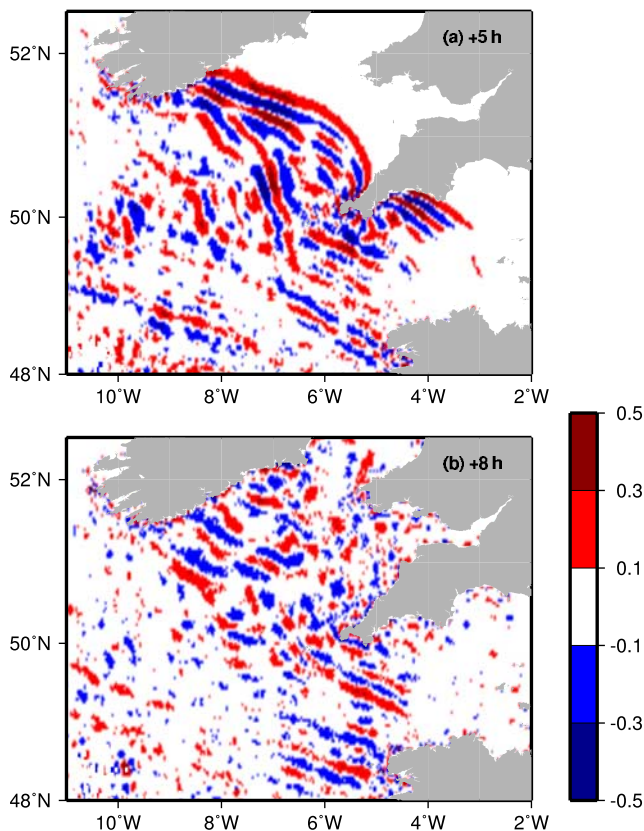
Figure 5. Surface elevation (m) in the inner finite element model, (a) 5 h and (b) 8 h after the disturbance for Run B2.

is usual to average equation (3) over at least one wave period; in the case of a tsunami propagating over a large distance the time bounds are not easily defined so we chose to average over 4 h, by which time the primary wave train has passed the U.K. shelf break. For Run B2 (Figure 9a) there was an asymmetrical energy flux in directions normal to the fault line and thence northwestward into the North Atlantic: a path with deeper bathymetry and fewer seamounts. Also, there was intensification of the energy flux over the Galician Rise and over the continental shelf in the Celtic Sea. This shows how the bathymetry acts as a waveguide, and also the energetic consequences resulting from interference due to shelf edge irregularities. As can be seen from equation (3), energy evolution at a point is controlled by the convergence of energy flux and dissipation (in shallow water). Figures 9b and 9c show how over the continental shelf, but away from the near-coast regions, the convergence term dominates the balance, with the frictional dissipation being an order of magnitude smaller.

[25] The time-averaged convergence of energy flux is an excellent indicator of those regions most important for transformations to the tsunami. The convergence (Figure 9b) is negative in the genesis region, where the time-mean potential energy has been reduced. There is positive convergence of energy flux along the axis normal to the fault line, which is consistent with the snapshots in Figure 4, where one can see the wavefront propagate in this direction. Away from the genesis region, there are finer-scale features in the energy flux convergence pattern, near Madeira, and

on the U.K. continental shelf. Here, the patterns of positive and negative flux convergence are aligned in the same direction as the beams of maximum elevation. The same interference pattern is seen in the frictional dissipation (Figure 9c) which is relatively large on the shelf break compared to elsewhere. To compare the temporal flux of energy at the shelf break with that closer to the shoreline, Figure 9d shows time series of the total energy per unit area averaged over the blue box (shelf break) and green box (inshore) marked on Figure 1a. The energy plot for the nearshore (green line) shows a factor of 2 amplification due to focusing effects, persists for several hours, and exhibits multiple peaks due to interference.

[26] For the run with a smoothed shelf edge the removal of topographic irregularities altered the interference pattern seen in the standard run, replacing it with a region of more uniform energy flux as shown in Figure 10a. Most of the energy flux convergence (Figure 10b) is now concentrated on the shelf edge without the multiple features seen in the standard run. It is important to note that even when the topographic irregularities are removed, the areas of maximum wave modification and energy dissipation are still some distance offshore. This is in contrast to the Iberian peninsula where the absence of a broad shelf means that modification is confined to a narrow coastal strip. In this way the wider continental shelf to the north provides a measure of protection by ensuring that significant energy transformations occur before the tsunami reaches the coast. Figure 10d shows that the energy flux time series across the two indicator regions is little altered when the shelf break is smoothed. The small-scale bathymetry may affect the pattern of interactions (Figure 10a) but it does not have any significant impact on the average shoreward energy transfer.

[27] Figure 11 illustrates the energy diagnostics when the Galician Rise was artificially removed. There is a reduction in flux magnitude where the Galician Rise once was, implying a focusing role for this feature in the standard run. The path of the energy flux is now more northward toward the U.K. shelf where the beams of energy flux (Figure 11a) have higher values than the previous runs (Figures 9a and 10a). This was confirmed by the energy time series (Figure 11d) where the peak energy arriving in the Bristol Channel increased by 20%, although paradoxically the flux of energy across the shelf break box was reduced. The Galician Rise therefore appears to protect the U.K. coastline from this scenario of tsunami impact in a complex way, through changing the flux convergence pattern in such a way that wave energy is more focused over that part of the shelf capable of reflecting and dissipating energy more efficiently.

5. Discussion

[28] We have examined six initial condition scenarios of tsunamis emanating from the Azores-Gibraltar Fault Zone and moving toward the northwest European continental shelf. The scenarios were guided by our best knowledge of the Lisbon tsunami of 1 November 1755, but the prime intention of this study was to explore the consequences and impacts in this region of such an event. As has been found previously [e.g., *Baptista et al.*, 1998b; *Mader*, 2001], modeling historical tsunami events is difficult as there is
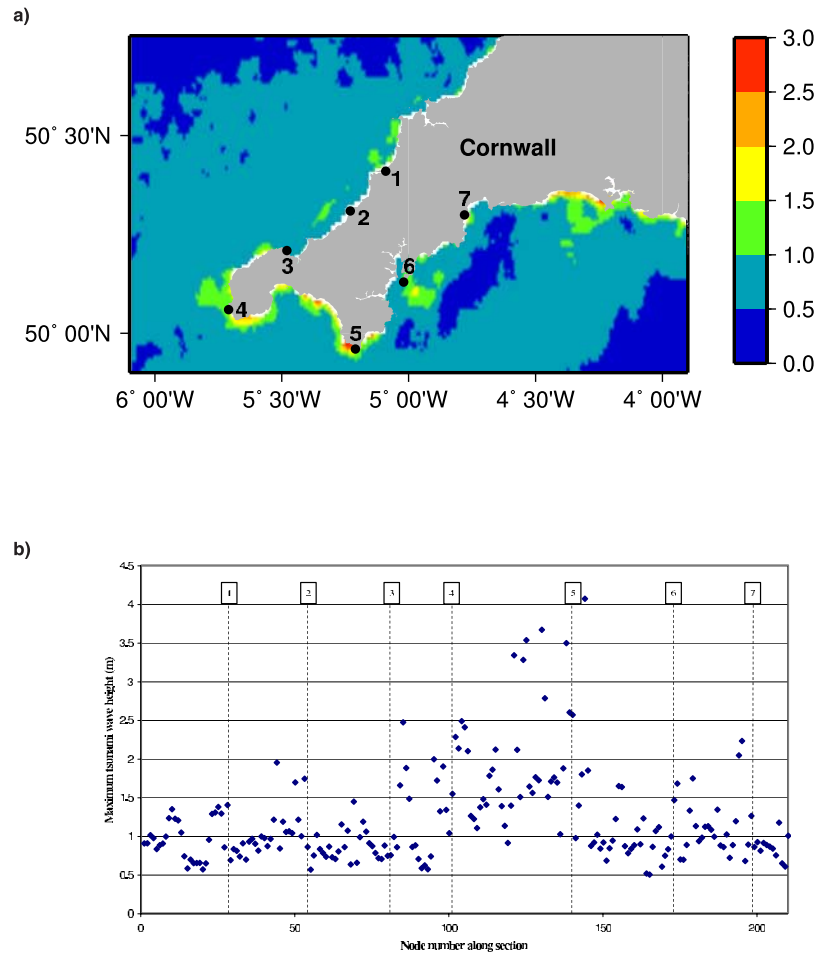
Figure 6. Maximum elevation (m) in the inner finite element model, (a) the region around Cornwall, SW England and (b) along the Cornish coast, with numbered points as shown in Figure 6a indicating distance along coast (upper abscissa label) and model node number (lower abscissa label).

usually a lack of trustworthy observations against which to verify. Our simulations illustrated several important aspects of interaction between a Lisbon-type tsunami and the topography of the northern European seaboard. We found that the impact of a 1755 type tsunami on northwest European shelf seas would be very sensitive to the location, orientation and magnitude of the initial seafloor deformation, with only one of our source models (B2) having any notable consequences. It is well known [e.g., *Titov et al.*, 2001] that the faulting location and the magnitude and extent of the seafloor displacement are the most important source parameters for determining the scale of far field effects. The subsequent wave evolution in our simulations was also sensitive to bathymetry, as has been shown previously by ray tracing studies [e.g., *Satake*, 1988] and by numerical modeling [e.g., *Titov et al.*, 2005]. In their global simulation of the 26 December 2004 Sumatra tsunami, *Titov et al.* [2005] found that wave directionality for that event was primarily controlled by source characteristics in the near field, and by topographic steering in the far field (where considerable amplification along ocean ridges was evident). Our results suggest that, for some events at least, there are scales at which these two primary controlling factors interact. The snapshots of surface elevation (Figure 4e)

show that the primary wave refracts around the Goban Spur, after which the two wavefronts interact with smaller topographic features producing beams of intensified elevation and wave energy flux on the U.K. shelf. These beams were present in both the finite difference and the higher-resolution finite element models.

[29] The maximum elevations obtained were approximately 3.5 m along the Cornish coast, but in the majority of places, maximum elevation was less than 1 m. These elevations are comparable to winter storm surge conditions, but unlike surge conditions there is extreme variability in the tsunami wave height from one location to another. Extreme sea levels resulting from this simulation (which represents the likely worst case for the United Kingdom), combined with both mean high-water spring (MHWS) and mean high-water neap (MHWN) tides, were calculated and compared with the 1:100 return level produced by *Dixon and Tawn* [1997]. The maximum elevations exceeded the 1:100 year extreme sea level only at three locations on the Cornish peninsula, and then only during MHWS tides. Elsewhere (and everywhere under MHWN conditions) the tsunami produced elevations similar to, or lower than, the predicted 1:100 year extreme sea level. The typical recurrence period for Lisbon style intraplate earthquakes is in the
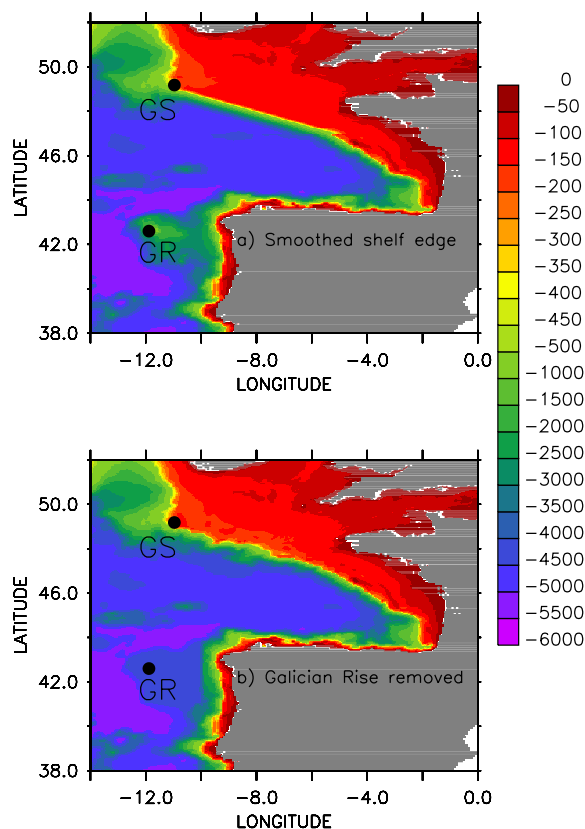
Figure 7. Modified bathymetry (m) for sensitivity experiments. (a) Smoothed version of the U.K. shelf edge, designed to have a constant along-slope profile with similar across-slope gradient to the real slope; (b) normal bathymetry but with the Galician Rise removed, with depths less than 4200 m being set to 4200 m in that vicinity. Key locations are annotated as for Figure 1.

range 1,000–10,000 years [*Gràcia et al.*, 2003; *Scholz et al.*, 1986]. The modeling supports the conclusion of *Kerridge et al.* [2005] that there is very low risk to the United Kingdom and northern Europe. Tsunami impact upon the Bristol Channel (a region of extremely high tides) was reduced since bathymetry-driven refraction directs any tsunami toward the north coast of Cornwall.

[30] In an experiment that smoothed the topographic irregularities at the shelf edge (Figure 8a) the multiple beams of high elevation disappeared, although a single beam still emanated from the Goban Spur. It seems reasonable to conclude that the former arose as a result of convergence and divergence over the many canyons known to exist in the shelf edge at this location. The amplification that remains with the smoothed bathymetry is probably due to interaction of the primary wave and a refracted wave at the sharp corner of the Goban Spur. In an independent experiment (Figure 8b), the topography of the Galician Rise above 4200 m was removed, allowing a more direct route for wave energy toward the European continental shelf. This caused an increase in the amplitude of the beams yet, paradoxically, reduced the energy flux over that part of the shelf facing the primary wave (Figure 11d). A possible explanation is that in the absence of the Galician Rise,

waves take a more direct route toward the Goban Spur where refraction redirects energy into the Celtic Sea. In any case, through complex interactions, the Galician Rise appears to shield the U.K. coastline from any tsunami on this trajectory. *Gjevik et al.* [1997] noted a similar effect due to the Gorringe Bank in their model of the 28 February 1969 tsunami, with a source south of the Horseshoe Abyssal Plain.

[31] For this particular event it appears that the wide European continental shelf provides a degree of protection to the coastline by reflecting and dissipating tsunami energy. The fact that frictional dissipation is an order of magnitude less than energy flux convergence at the shelf break (Figures 9–11c) implies that reflection and scattering are more important than frictional dissipation here. In contrast, on the Iberian peninsula (which has only a narrow shelf), energy transformations do not occur until waves are very
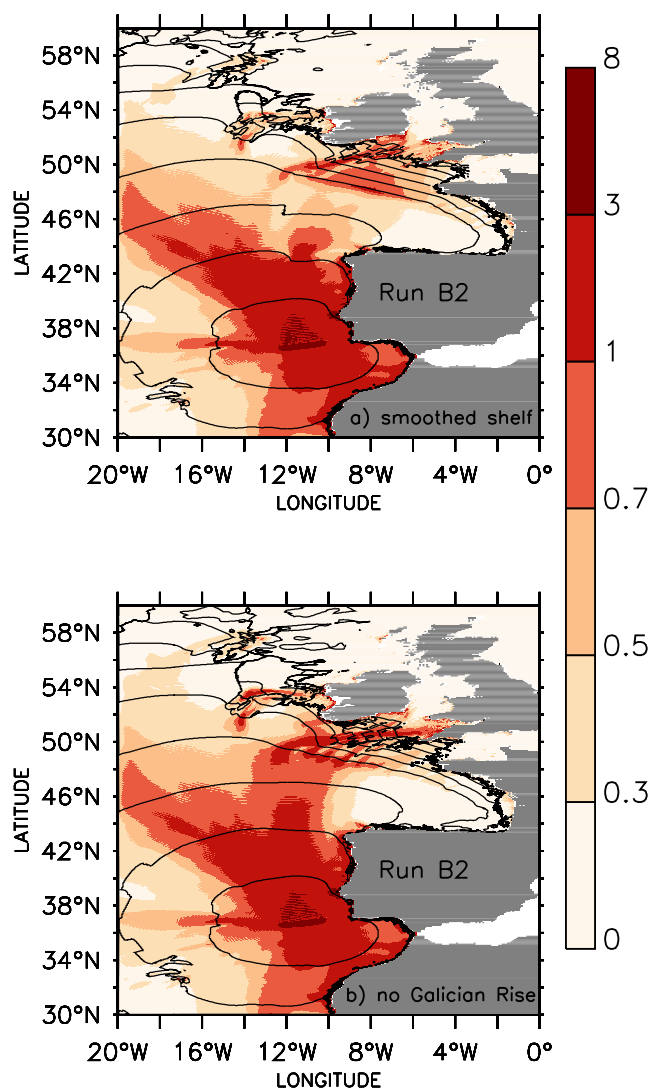
Figure 8. Maximum sea surface elevation during the first 12 h (shaded, m) and arrival time of maximum for the first 6 h (contours, 0.5 h contour interval) for sensitivity experiments based on scenario B2. (a) With smoothed U.K. shelf edge bathymetry; (b) normal bathymetry but with Galician Rise removed.
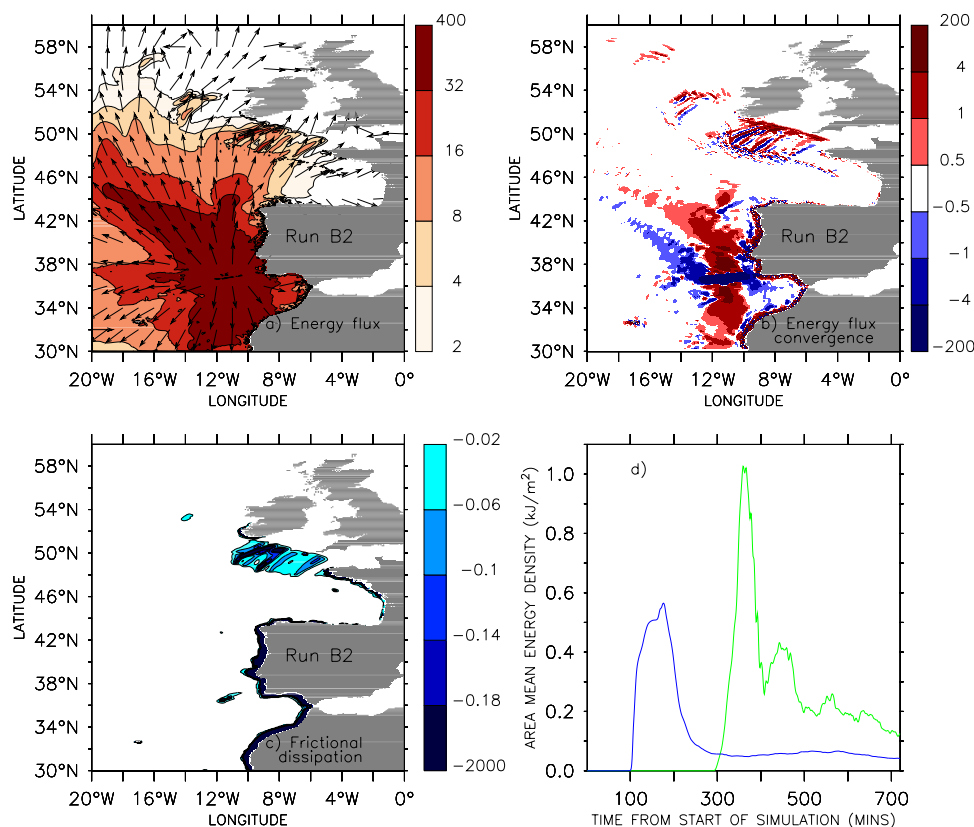
Figure 9. Energy diagnostics for the B2 run. (a) Time-mean of magnitude (shaded, 10^3 Wm^{-1}) and direction (unit vectors) of the depth-integrated energy flux, $\mathbf{F_E}$; (b) time-mean of convergence of the depth-integrated energy flux, $-\nabla_S \cdot \mathbf{F_E}$ (shaded, 10^{-5} Wm^{-2}); (c) time-mean of depth-integrated frictional dissipation of energy through bottom drag, $-\rho\gamma|\mathbf{u}|^3$ (shaded, 10^{-5} Wm^{-2}); (d) time series of the area-mean of total energy per unit horizontal area, E (10^3 Jm^{-2}), for the regions shown by blue and green rectangles in Figure 1a.

close to the coastline, producing more severe impacts; along the Iberian and African coastlines the frictional dissipation term is far higher than elsewhere and is confined to a narrow coastal strip. The shallow water on broad shelves also reduces the tsunami phase speed, on the one hand giving more lead time for tsunami warning, but also potentially allowing the wavelength to match critical topographic scales and give rise to amplifying interactions. Our results show significant local reamplification due to shoaling and resonance. There is still much energy in the Celtic Sea after 8 h, as seen in Figure 5b, and this slow decay of energy is consistent with other studies: *Fine et al.* [2005] stated that local differences in Q-factor and wave period are topographically induced, and *Titov et al.* [2005] also noted prolonged ringing after multiple topographic interactions. Our results (Figure 6) illustrate a high degree of variability in maximum wave amplitude around that part of the coastline most affected by the waves. Calculations of the Q-factor, based on time series for locations 5 and 7 in Figure 6a, and using the methodology of *Kulikov et al.* [1996], gave values of 13. This is indicative of a strong resonant response on the shelf, and although we see high variability in wave amplitude, the decay characteristics are more spatially uniform, suggesting that the ringing is set up over the wider shelf rather than in specific localities. Our energy time series are consistent with this, showing the area-mean energy

density in the selected nearshore region (the green line in Figures 9–11d) to decay fairly slowly. This pattern of decay was insensitive to the bathymetric experiments we performed and instead reflects the resonant behavior of the designated area. Our results illustrate how, in subtle ways, bathymetric features have the potential to both increase and decrease the hazard resulting from tsunamis.

[32] NLSW models are generally considered to be a suitable choice for propagating tsunamis of seismic origin, where the sea surface deformation responds almost instantaneously to seafloor movement and frequency dispersion can be ignored in the generation region. They are not suitable for shorter-wavelength tsunamis (e.g., those generated by submarine landslides), where dispersive effects are required and Boussinesq equation models are more accurate [*Lynett and Liu*, 2002]. Frequency dispersion can also be important when tsunamis propagate over long distances. The 26 December 2004 Sumatra tsunami generated a wealth of observational evidence and prompted a reevaluation of modeling techniques. Wavelet analysis on altimetry data [*Kulikov*, 2006] showed that the high-frequency components of the tsunami, with approximately 10 km wavelength, were distinctly dispersive. This suggests that frequency dispersion may be a necessary ingredient of numerical models used for the transoceanic propagation of tsunamis [*Grilli et al.*, 2006]. Highly nonlinear Boussinesq-
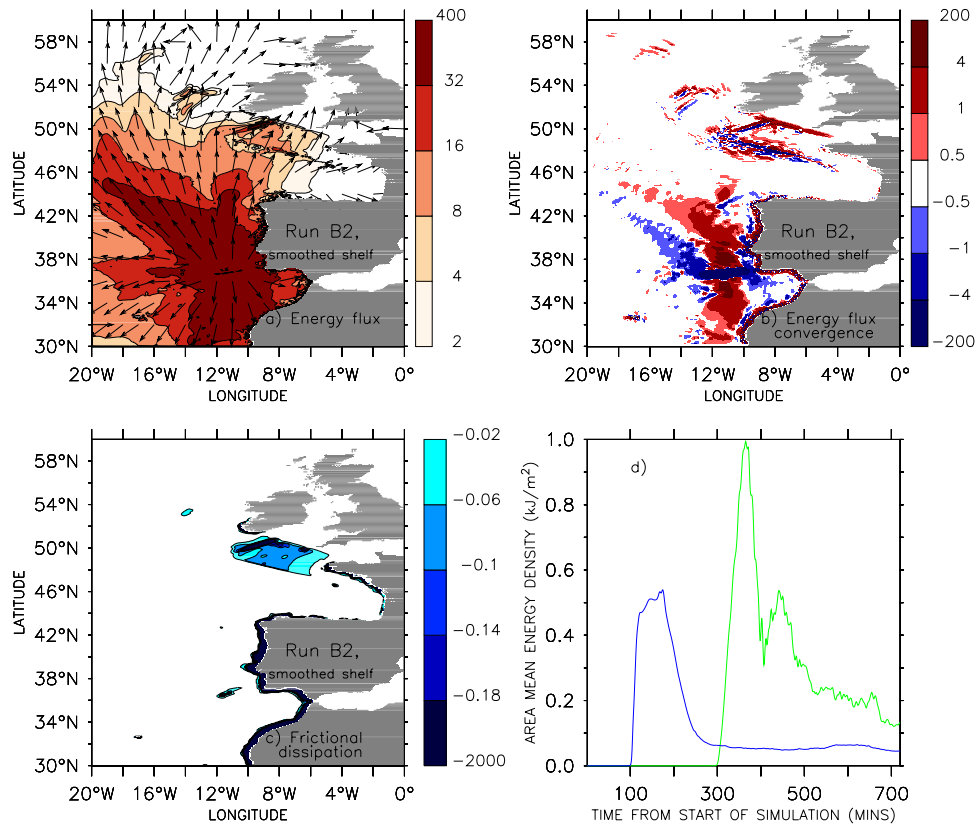
Figure 10. Energy diagnostics for the B2 run, with smoothed U.K. shelf edge bathymetry as shown in Figure 7a. Caption as for Figure 9.
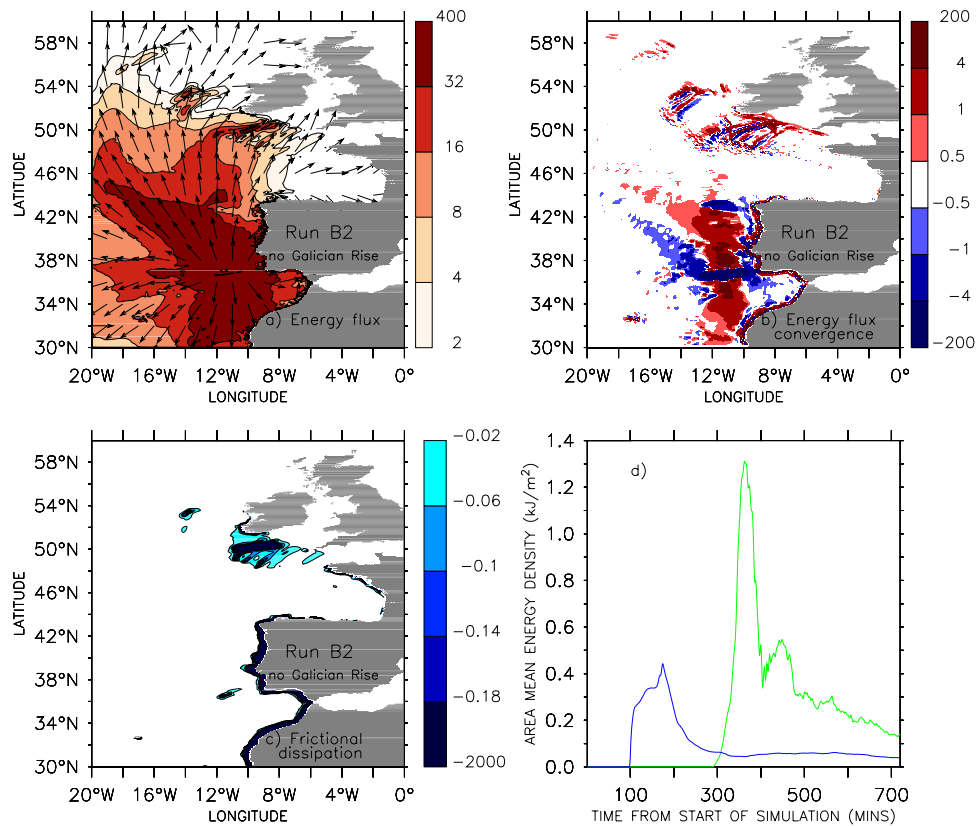
Figure 11. Time-mean energy diagnostics for the B2 run, with normal bathymetry but with Galician Rise removed, as shown in Figure 7b. Caption as for Figure 9.

type models [e.g., *Wei et al.*, 1995] are now capable of simulating frequency dispersion faithfully in intermediate depths. With a suitable treatment of the moving shoreline boundary [e.g., *Lynett et al.*, 2002] these models produce accurate wave runup when compared to analytical and experimental solutions. *Ioualalen et al.* [2007] have recently used the FUNWAVE model [*Chen et al.*, 2000] to simulate runup in Thailand following the 26 December 2004 tsunami and achieved excellent agreement with 58 sets of observations. The advantage of this approach is that a single model with the most appropriate physics can be used to simulate tsunami behavior from source to beach.

[33] This study reinforces the scale of the inherent uncertainties when attempting to model tsunami risk in regions where the consequences of tsunamigenic earthquakes are more likely to be felt. Although the physics of these uncertainties are well known, they must be correctly accounted for in a sufficiently large ensemble if maximum benefit is to be gained from tsunami modeling. Indeed, in our study, because of the subsequent interaction with bathymetry it may be that only very small changes in the source model fault orientations could have yielded significantly different results. The choice of (time integrated) energy flux divergence as a diagnostic variable is seen to be useful when identifying regions of significant wave transformation. The divergence of energy flux can reveal regions of transformation that are not apparent when looking at energy flux itself. This could be useful, for instance, when comparing various model runs in risk assessment studies.

References

Abe, K. (1979), Size of great earthquakes of 1837–1974 inferred from tsunami data, *J. Geophys. Res.*, 84, 1561–1568.

Baptista, M. A., S. Heitor, J. M. Miranda, P. M. A. Miranda, and L. Mendes Victor (1998a), The 1755 Lisbon tsunami: Evaluation of the tsunami parameters, *J. Geodyn.*, 25, 143–157.

Baptista, M. A., P. M. A. Miranda, J. M. Miranda, and L. Mendes Victor (1998b), Constrains on the source of the 1755 Lisbon tsunami inferred from numerical modelling of historical data on the source of the 1755 Lisbon tsunami, *J. Geodyn.*, 25, 159–174.

Bondevik, S., J. I. Svendsen, G. Johnsen, J. Mangerud, and P. E. Kaland (1997), The Storegga tsunami along the Norwegian coast, its age and runup, *Boreas*, 26, 29–53.

Borlase, W. (1755), Letter to the Rev. Charles Lytteton, *Phil. Trans. R. Soc. London*, 49, 373–378.

Chen, Q., J. T. Kirby, R. A. Dalrymple, A. B. Kennedy, and A. Chawla (2000), Boussinesq modeling of wave transformation, breaking, and runup. II: 2D, *J. Waterway Port Coast. Ocean Eng.*, 126(1), 48–56.

Choi, B. H., E. Pelinovsky, S. J. Hong, and S. B. Woo (2003), Computation of tsunamis in the East (Japan) Sea using dynamically interfaced nested model, *Pure Appl. Geophys.*, 160, 1383–1414.

Davies, A. M., and S. C. M. Kwong (2000), Tidal energy fluxes and dissipation on the European continental shelf, *J. Geophys. Res.*, 105(C3), 21,969–21,989.

Dawson, A. G., R. M. W. Musson, I. D. L. Foster, and D. Brunsden (2000), Abnormal historic sea-surface fluctuations, SW England, *Mar. Geol.*, 170, 59–68.

Dixon, M. J., and J. A. Tawn (1997), Spatial analyses for the UK coast, *Internal Doc.*, 112, 217 pp., Proudman Oceanogr. Lab., Liverpool, UK.

Fine, I. V., A. B. Rabinovich, B. D. Bornhold, and R. E. Thomson (2005), The Grand Banks landslide-generated tsunami of November 18, 1929: Preliminary analysis and numerical modeling, *Mar. Geol.*, 215, 45–57.

Flather, R. A. (1976), A tidal model of the north-west European continental shelf, *Mem. Soc. R. Sci. Liege*, 6, 141–164.

Flather, R. A. (2000), Existing operational oceanography, *Coastal Eng.*, 41, 13–40.

Fukao, Y. (1973), Thrust faulting at a lithospheric plate boundary: The Portugal earthquake of 1969, *Earth Planet. Sci. Lett.*, 18, 205–216.

Galland, J. C., N. Goutal, and J. M. Hervouet (1991), TELEMAC: A new numerical model for solving shallow-water equations, *Adv. Water Resour.*, 14, 138–148.

Gjevik, B., G. Pederson, E. Dybesland, C. B. Harbitz, P. M. A. Miranda, M. A. Baptista, L. Mendes-Victor, P. Heinrich, R. Roche, and M. Guesmia (1997), Modeling tsunamis from earthquake sources near Gorringe Bank southwest of Portugal, *J. Geophys. Res.*, 102(C13), 27,931–27,949.

Gràcia, E., J. Dañobeitia, J. Vergés, and the PARSIFAL team (2003), Mapping active faults offshore Portugal (36°N–38°N): implications for seismic hazard assessment along the southwest Iberia margin, *Geology*, 31, 83–86.

Grilli, S. T., A. M. Baptista, M. Ioualalen, J. Asavanant, J. T. Kirby, F. Shi, and Y. L. Zhang (2006), Effects of frequency dispersion on tsunami propagation and coastal impact, *Geophys. Res. Abstr.*, 8, 09021.

Gutscher, M. A. (2004), What caused the Great Lisbon earthquake?, *Science*, 305, 1247–1248.

Henni, P. H. O., C. J. Fyfe, and P. C. Marrow (1998), The BGS World Seismicity Database, *Brit. Geol. Surv. Tech. Rep. WL/98/13*, internal document, 12 pp., Brit. Geol. Surv., Edinburgh.

Hervouet, J.-M. (2000a), TELEMAC modelling system: An overview, *Hydrol. Proc.*, 14, 2209–2210.

Hervouet, J. M. (2000b), A high resolution 2-D dam-break model using parallelization, *Hydrol. Proc.*, 14, 2211–2230.

Ioualalen, M., J. A. Asavanant, N. Kaewbanjak, S. T. Grilli, J. T. Kirby, and P. Watts (2007), Modeling of the 26th December 2004 Indian Ocean tsunami: Case study of impact in Thailand, *J. Geophys. Res.*, 112, C07024, doi:10.1029/2006JC003850.

Johnston, A. C. (1996), Seismic moment assessment of earthquakes in stable continental regions: III. New Madrid 1811–1812, Charleston 1886 and Lisbon 1755, *Geophys. J. Int.*, 126, 314–344.

Jones, J. E., and A. M. Davies (2005), An intercomparison between finite difference and finite element (TELEMAC) approaches to modelling west coast of Britain tides, *Ocean Dyn.*, 55, 178–198.

Jones, J. E., and A. M. Davies (2006), Application of a finite element model (TELEMAC) to computing the wind induced response of the Irish Sea, *Cont. Shelf Res.*, 26, 1519–1541.

Kanamori, H. (2006), Lessons from the 2004 Sumatra-Andaman earthquake, *Phil. Trans. R. Soc. A*, 364, 1927–1945.

Kerridge, D., et al. (2005), The threat posed by tsunami to the UK, study commissioned by Defra Flood Management Division, 165 pp., Dept. for Environ. Food and Rural Affairs, London.

Kowalik, Z. (2001), Basic relations between tsunami calculation and their physics, *Sci. Tsunami Hazards*, 5(2), 77–84.

Kulikov, E. A. (2006), Dispersion of the Sumatra tsunami waves in the Indian Ocean detected by satellite altimetry, *Russ. J. Earth Sci.*, 8, ES4004, doi:10.2205/2006ES000214.

Kulikov, E. A., A. B. Rabinovich, R. E. Thomson, and B. D. Bornhold (1996), The landslide tsunami of November 3 1994, Skagaway Harbor, Alaska, *J. Geophys. Res.*, 101(C3), 6609–6615.

Lynett, P. J., and P.L.-F. Liu (2002), A numerical study of submarine-landslide-generated waves and runup, *Proc. R. Soc. London, Ser. A.*, 458, 2885–2910.

Lynett, P. J., T. R. Wu, and P. L.-F. Liu (2002), Modelling wave runup with depth-integrated equations, *Coastal Eng.*, 46(2), 89–107.

Machado, F. (1966), Contribuicao para o estudo do terramoto de 1 de Novembro de 1755, *Rev. Faculdade Cienc. Lisboa*, 14, 19–31.

Mader, C. L. (2001), Modeling the 1755 Lisbon tsunami, *Sci. Tsunami Hazards*, 19, 93–98.

Malcherek, A. (2000), Application of TELEMAC-2D in a narrow estuarine tributary, *Hydrol. Proc.*, 14, 2293–2300.

Mendes, V. L., M. A. Baptista, J. M. Miranda, and P. M. A. Miranda (1999), Can hydrodynamic modelling of tsunami contribute to seismic risk assessment?, *Phys. Chem. Earth A*, 24, 139–144.

Moreira, V. S. (1989), Seismicity of the Portuguese continental margin, in *Earthquakes at North Atlantic Passive Margins Neotectonic and Postglacial Rebound*, edited by S. Gregersen and P. W. Basham, Kluwer, Mass.

Okada, Y. (1985), Surface deformation due to shear and tensile faults in a half-space, *Bull. Seismol. Soc. Am.*, 75, 1135–1154.

Pires, C., and P. M. A. Miranda (2001), Tsunami waveform inversion by adjoint methods, *J. Geophys. Res.*, 106(C9), 19,773–19,796.

Reid, H. F. (1914), The Lisbon earthquake of November 1 1755, *Bull. Seismol. Soc. Am.*, 4, 53–80.

Rise, L., D. Ottesen, K. Berg, and E. Lundin (2005), Large-scale development of the mid-Norwegian margin during the last 3 million years, *Mar. Pet. Geol.*, 22, 33–44.

Satake, K. (1988), Effects of bathymetry on tsunami propagation: Application of ray tracing to tsunamis, *Pure Appl. Geophys.*, *126*, 27–36.

Sauvaget, P., E. David, and C. G. Soares (2000), Modelling tidal currents on the coast of Portugal, *Coastal Eng.*, *40*(4), 393–409.

Scholz, C. H. (2002), *The Mechanics of Earthquake Faulting*, 2nd ed., 496 pp., Cambridge Univ. Press, Cambridge, UK.

Scholz, C. H., C. A. Aviles, and S. G. Wesnousky (1986), Scaling differences between large interplate and intraplate earthquakes, *Bull. Seismol. Soc. Am.*, *76*, 65–70.

Shuto, N. (1991), Numerical simulation of tsunamis: Its present and near future, *Natural Hazards*, *4*, 171–191.

Smith, D. E., et al. (2004), The Holocene Storegga slide in the United Kingdom, *Quat. Sci. Rev.*, *23*, 2291–2321.

Soulsby, R. (1998), *Dynamics of Marine Sands*, 272 pp., Thomas Telford, London.

Stich, D., F. L. de Mancilla, and J. Morales (2005), Crust-mantle coupling in the Gulf of Cadiz (SW-Iberia), *Geophys. Res. Lett.*, *32*, L13306, doi:10.1029/2005GL023098.

Titov, V. V., and F. I. Gonzalez (1997), Implementation and testing of the Method of Splitting Tsunami (MOST) model, *NOAA Tech. Mem.*, *ERL PMEL-112*, 11 pp., NOAA Pac. Mar. Environ. Lab., Seattle, Wash.

Titov, V. V., H. O. Mofjeld, F. I. Gonzalez, and J. C. Newman (2001), Offshore forecasting of Alaskan tsunamis in Hawaii, in *Tsunami Research at the End of a Critical Decade*, edited by G. T. Hebenstreit, pp. 75–90, Kluwer Acad., Amsterdam.

Titov, V. V., A. B. Rabinovich, H. O. Mofjeld, R. E. Thomson, and F. I. Gonzalez (2005), The global reach of the 26 December 2004 Sumatra tsunami, *Science*, *309*, 2045–2048.

Vilanova, S. P., C. F. Nunes, and F. B. D. J.Fonseca (2003), Lisbon 1755 A case of triggered onshore rupture?, *Bull. Seismol. Soc. Am.*, *93*, 2056–2068.

Wei, G., J. T. Kirby, S. T. Grilli, and R. Subramanya (1995), A fully nonlinear Boussinesq model for surface waves: I. Highly nonlinear, unsteady waves, *J. Fluid Mech.*, *294*, 71–92.

Zitellini, N., F. Chierici, R. Sartori, and L. Torelli (1999), The tectonic source of the 1755 earthquake and tsunami, *Ann. Geofis.*, *42*, 49–55.

Zitellini, N., et al. (2001), Source of the 1755 Lisbon earthquake and tsunami investigated, *EOS Trans. AGU*, *82*, 290–291.

————————————

B. J. Baptie, R. M. W. Musson, L. Ottemöller, and S. L. Sargeant, British Geological Survey, Edinburgh EH9 3LA, UK.

A. Cooper, D. Cresswell, and S. Richardson, HR Wallingford, Wallingford OX10 8BA, UK.

K. J. Horsburgh and C. Wilson, Proudman Oceanographic Laboratory, Liverpool L3 5DA, UK.